Classical and Quantum Gravity

High-accuracy numerical models of Brownian thermal noise in thin mirror coatings

To cite this article: Nils L Vu *et al* 2023 *Class. Quantum Grav.* **40** 025015

OPEN ACCESS
IOP Publishing
Classical and Quantum Gravity
Class. Quantum Grav. 40 (2023) 025015 (15pp)
https://doi.org/10.1088/1361-6382/acad62

High-accuracy numerical models of Brownian thermal noise in thin mirror coatings

Nils L Vu[1,4,*], Samuel Rodriguez[2,3], Tom Włodarczyk[1], Geoffrey Lovelace[2], Harald P Pfeiffer[1], Gabriel S Bonilla[2], Nils Deppe[4], François Hébert[4], Lawrence E Kidder[5], Jordan Moxon[4] and William Throwe[5]

[1] Max Planck Institute for Gravitational Physics (Albert Einstein Institute), Am Mühlenberg 1, Potsdam 14476, Germany
[2] Nicholas and Lee Begovich Center for Gravitational-Wave Physics and Astronomy, California State University Fullerton, Fullerton, CA 92831, United States of America
[3] Department of Physics and Astronomy, University of Mississippi, University, MS 38677, United States of America
[4] Theoretical Astrophysics, Walter Burke Institute for Theoretical Physics, California Institute of Technology, Pasadena, CA 91125, United States of America
[5] Cornell Center for Astrophysics and Planetary Science, Cornell University, Ithaca, NY 14853, United States of America

E-mail: owls@nilsvu.de

Received 23 August 2022; revised 9 December 2022
Accepted for publication 20 December 2022
Published 3 January 2023

Abstract

Brownian coating thermal noise in detector test masses is limiting the sensitivity of current gravitational-wave detectors on Earth. Therefore, accurate numerical models can inform the ongoing effort to minimize Brownian coating thermal noise in current and future gravitational-wave detectors. Such numerical models typically require significant computational resources and time, and often involve closed-source commercial codes. In contrast, open-source codes give complete visibility and control of the simulated physics, enable direct assessment of the numerical accuracy, and support the reproducibility of results. In this article, we use the open-source `SpECTRE` numerical relativity code and

---

[*] Author to whom any correspondence should be addressed.

adopt a novel discontinuous Galerkin numerical method to model Brownian coating thermal noise. We demonstrate that `SpECTRE` achieves significantly higher accuracy than a previous approach at a fraction of the computational cost. Furthermore, we numerically model Brownian coating thermal noise in multiple sub-wavelength crystalline coating layers for the first time. Our new numerical method has the potential to enable fast exploration of realistic mirror configurations, and hence to guide the search for optimal mirror geometries, beam shapes and coating materials for gravitational-wave detectors.

Supplementary material for this article is available online

Keywords: gravitational-wave detectors, brownian coating thermal noise, numerical simulation, discontinuous Galerkin methods

(Some figures may appear in colour only in the online journal)

1. Introduction

Brownian coating thermal noise is the limiting noise source for current-generation, ground-based gravitational-wave detectors in their most sensitive frequency bands. For instance, following the A+ upgrade anticipated for completion in the mid 2020s, the Laser Interferometer Gravitational-Wave Observatory (LIGO) detector noise is dominated by Brownian coating thermal noise at frequencies $f \sim 100$ Hz [1]. This noise arises from thermal fluctuations in the reflective coatings of the detectors' test masses [2].

Therefore, a reduction of the Brownian coating thermal noise directly increases a detector's sensitivity and thus its astronomical reach. Theoretical models of Brownian coating thermal noise are important for working toward this goal. Thermal noise modeling typically follow the approach pioneered by Levin [3], which computes the thermal noise in terms of an auxiliary elasticity calculation using the fluctuation-dissipation theorem [4–6]. While an approximate analytic solution is well known in the limit where coating thickness and edge effects can be neglected, numerical calculations of thermal noise are necessary to study effects that arise from the finite test-mass size, the finite coating thickness, and from crystalline materials.

In this article we calculate Brownian coating thermal noise by numerically solving the auxiliary linear elasticity problem. Such numerical simulations typically adopt a conventional finite-element approach, as some of the authors did in [7]. These methods are widely used, but achieving high accuracy with them can require significant computational resources and time, because of their relatively slow rates of convergence.

For the first time to our knowledge, we apply a discontinuous Galerkin (DG) method to model Brownian coating thermal noise. DG methods are well suited to this problem because they can retain high-order convergence in the presence of discontinuities, which arise at the interfaces between the mirror substrate and its reflective coatings. In this article, we extend the DG method for elliptic equations presented in [8] to problems with discontinuous material properties. With this extension, our method converges exponentially with resolution, allowing us to solve coating thermal noise problems numerically at high accuracy using considerably less computational resources and time than conventional finite-element methods.

We implement the numerical method and the elastostatic equations in `SpECTRE` [9], a new open-source numerical relativity code. While `SpECTRE`'s primary aim is to model merging black holes and neutron stars, the elliptic solver needed to construct initial data for such simulations is also very well positioned to solve the DG-discretized elastostatics equations for thermal noise modeling [8, 10]. As an open-source code, our approach has advantages compared to the closed-source and commercial solutions that are often adopted: we can directly control the physics incorporated in the calculation, we can assess the accuracy and convergence rate of our simulations in a straightforward way, and our results are reproducible with publicly available software. Our code also benefits from `SpECTRE`'s task-based parallelism approach, implemented using the `Charm++` [11] library, enabling our code to efficiently scale to large numbers of compute cores [12].

This article is organized as follows. Section 2 summarizes the elastic problem to be solved and presents the DG numerical method. Section 3 presents our results using this method to model thermal noise in cylindrical mirrors with thin coatings. We discuss our results and future work in section 4.

2. Methods

In this section, we formulate the auxiliary elasticity problem based on [3, 7], discretize it with the DG scheme developed in [8], and outline the numerical method we employ to solve the discretized problem with the `SpECTRE` code [10]. Section 2.2.3 details a novel extension of this method to handle discontinuous material properties at layer interfaces.

2.1. Auxiliary elasticity problem

We consider a gravitational-wave detector that measures the position of a test mass with a laser beam with a Gaussian intensity profile

$$p(r) = \frac{1}{\pi r_0^2} e^{-r^2/r_0^2}. \tag{1}$$

Here, r is the cylindrical radial coordinate from the center of the beam with width r_0. The intensity profile is normalized so that

$$\int_0^{2\pi} \mathrm{d}\phi \int_0^{\infty} \mathrm{d}r\, r p(r) = 1. \tag{2}$$

The laser beam effectively measures a weighted average q of the displacement Z of the test mass surface,

$$q(t) = \int_0^{2\pi} \mathrm{d}\phi \int_0^{R} \mathrm{d}r\, r p(r,\phi) Z(r,\phi,t). \tag{3}$$

As shown by Levin [3], Brownian thermal noise can be calculated from the energy dissipated in an auxiliary elastic problem. Specifically, to compute the thermal noise at frequency f, one applies an oscillating pressure to the face of the mirror with frequency f, with a pressure distribution profile $p(r)$ equal to the beam intensity, and with an amplitude F_0. In this auxiliary problem, the energy W_{diss} will be dissipated in each cycle of the oscillation. The fluctuation-dissipation theorem relates this dissipated energy W_{diss} to the thermal noise, specifically to the power spectral density S_q associated with q,[6]

$$S_q = \frac{2 k_{\mathrm{B}} T}{\pi^2 f^2} \frac{W_{\mathrm{diss}}}{F_0^2}, \tag{4}$$

where T is the mirror temperature and k_{B} is Boltzmann's constant. Because $W_{\mathrm{diss}} \propto F_0^2$, it follows that S_q does not depend on the overall amplitude F_0.

---

[6] See, e.g. equation (11.90) in [13].

For frequencies $f \sim 100$ Hz much lower than the resonant frequencies $f \sim 10^4$ Hz of the test-mass materials, the dissipated power can be computed using the quasistatic approximation. In this approximation, a static pressure is applied to the mirror with amplitude F_0 and profile $p(r)$, and the dissipated energy can be written as

$$W_{\text{diss}} = U\phi, \tag{5}$$

where U is the potential energy stored in the deformation of the test-mass and ϕ is the material's loss angle determined by the material's imaginary, dissipative elastic moduli.

Therefore, our goal in this article is to solve the equations of elastostatics for the deformation of the test mass,

$$\nabla_i T^{ij} = f^j(\boldsymbol{x}), \tag{6}$$

when its surface is subjected to an applied pressure with profile $p(r)$. Here, T^{ij} is the *stress* and we adopt the Einstein summation convention so that repeated tensor indices are summed over. The source f^j is the force density acting on each volume element of the mirror as a function of position $\boldsymbol{x}$, which vanishes in our situation, $f^j = 0$. The pressure acting on the external surface of the test mass will be represented by suitable boundary conditions.

Equation (6) is an equation for the *displacement vector field* $u^i(\boldsymbol{x})$, which describes the deformation of the elastic material as a function of the undeformed coordinates. The symmetric part of the gradient of the displacement vector field is the *strain*

$$S_{kl} = \nabla_{(k} u_{l)}. \tag{7}$$

For sufficiently small F_0, the strain is proportional to the applied stress,

$$T^{ij} = -Y^{ijkl} S_{kl}, \tag{8}$$

where the *constitutive relation* $Y^{ijkl}(\boldsymbol{x})$ captures the elastic properties of the material in the linear regime. The constitutive relation is symmetric on its first two indices, on its last two indices, and under exchange of the first pair of indices with the second pair of indices.

Inserting equations (7) and (8) into equation (6) yields the equations of linear elasticity,

$$-\nabla_i Y^{ijkl} \nabla_{(k} u_{l)} = f^j(\boldsymbol{x}), \tag{9}$$

which we will solve numerically.

We consider materials with either amorphous or cubic-crystalline constitutive relations. The coating may consist of only a single material, or of multiple layers with different materials. The amorphous constitutive relation is isotropic and homogeneous,

$$Y^{ijkl} = \lambda \delta^{ij} \delta^{kl} + \mu \left(\delta^{ik} \delta^{jl} + \delta^{il} \delta^{jk} \right), \tag{10}$$

with *Lamé parameter* λ and *shear modulus* μ.[7] A cubic-crystalline material is characterized by the constitutive relation

$$Y^{ijkl} = \begin{cases} c_{11} & \text{for } i = j = k = l \\ c_{12} & \text{for } i = j, k = l, i \neq k \\ c_{44} & \text{for } i = k, j = l, i \neq j \text{ or } i = l, j = k, i \neq j \end{cases} \tag{11}$$

---

[7] The Lamé parameter can also be replaced by the *bulk modulus* $K = \lambda + 2\mu/3$. Alternatively, the two parameters can be replaced by the *Young's modulus* $Y = 9K\mu/(3K + \mu) = \mu(3\lambda + 2\mu)/(\lambda + \mu)$ and the *Poisson ratio* $\sigma = (3K - 2\mu)/(2(3K + \mu)) = \lambda/(2(\lambda + \mu))$.

where c_{11}, c_{12} and c_{44} are three independent material parameters. The constitutive relation in equation (9) is composed by discontinuously choosing either equation (10) or equation (11) in each layer of the material.

After solving the linear elasticity equations, equation (9), the potential energy is evaluated by an integral over the volume of the material,

$$U = -\frac{1}{2}\int_V dV S_{ij} T^{ij}. \tag{12}$$

For a material with a thin, reflective coating with different elastic properties than the substrate, the dissipated energy, equation (5), decomposes as [14]

$$W_{\mathrm{diss}} = U_{\mathrm{sub}}\,\phi_{\mathrm{sub}} + U_{\mathrm{coat}}\,\phi_{\mathrm{coat}}, \tag{13}$$

where U_{sub} and ϕ_{sub} are the potential energy and loss angle of the substrate, respectively, while U_{coat} and ϕ_{coat} are the potential energy and the loss angle of the coating. Note that a material can also have different loss angles associated with the different independent elastic moduli of a material [15]. We do not consider further decompositions of the elastic potential energy in this article, but note that such quantities can straightforwardly be extracted from our simulations. The different loss angles only affect the computation of the thermal noise by equation (4) from the elastic potential energy extracted from our simulations, but they do not affect our simulations or our numerical method in any way.

An approximate analytic solution exists for amorphous materials in the limit where the coating thickness d is small compared to both the size of the mirror and the width r_0 of the pressure profile. The approximate coating thermal noise is[8]

$$S_q^{\mathrm{coat}} = \frac{k_{\mathrm{B}}T}{\pi^2 f}\frac{1-\sigma_{\mathrm{sub}}^2}{r_0 Y_{\mathrm{sub}}}\frac{d}{r_0}\frac{\phi_{\mathrm{coat}}}{Y_{\mathrm{sub}}Y_{\mathrm{coat}}(1-\sigma_{\mathrm{coat}}^2)(1-\sigma_{\mathrm{sub}}^2)} \times \left(Y_{\mathrm{coat}}^2(1+\sigma_{\mathrm{sub}})^2(1-2\sigma_{\mathrm{sub}})^2 + Y_{\mathrm{sub}}^2(1+\sigma_{\mathrm{coat}})^2(1-2\sigma_{\mathrm{coat}})\right). \tag{14}$$

2.2. DG discretization

We employ the DG scheme detailed in [8] to discretize the elasticity problem, equation (9). We summarize the discretization scheme in this section, and extend it to problems with discontinuous material properties.

2.2.1. Domain decomposition. We simulate a cylindrical mirror in three dimensions with radius R and height H. The cylinder axis coincides with the z axis of our coordinates, and the plane $z=0$ represents the surface of the mirror on which the external pressure $p(r)$ is applied. We decompose the cylindrical domain $\Omega = [0,R]\times[0,2\pi)\times[0,H]$ into a set of nonoverlapping elements $\Omega_k \subset \Omega$ shaped like deformed cubes, as illustrated in figure 1(a) (h refinement). Each element carries a coordinate map from the Cartesian coordinates $\boldsymbol{x}\in\Omega_k$, in which the elasticity equation (9) are formulated, to *logical* coordinates $\boldsymbol{\xi}\in[-1,1]^3$ representing the reference cube, as illustrated in figure 1(b). The coordinate map to the reference cube is characterized by its Jacobian,

$$\mathrm{J}^i_j = \frac{\partial x^i}{\partial \xi^j} \tag{15}$$

---

[8] See equation (22) in [14], where $w=\sqrt{2}r_0$, $\phi_{||}=\phi_\phi=\phi_{\mathrm{coat}}$, and we consider only the coating contribution.

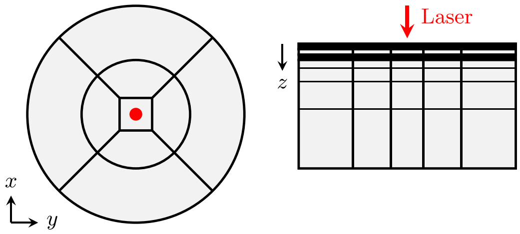

(a) Domain

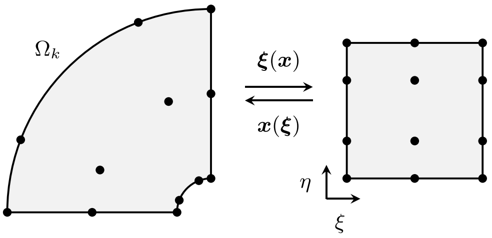

(b) Element

Figure 1. Top: geometry of our layered cylindrical domain, with the laser beam indicated in red. Four wedge-shaped elements envelop a cuboid. Another set of wedges extends to the outer radius of the cylinder. In z direction the cylinder is partitioned into layers that can have different material properties (black and gray). The substrate layer has a logarithmic coordinate map in z direction and is split in two twice in this example (thin horizontal lines). Bottom: the coordinate transformation $\boldsymbol{\xi}(\boldsymbol{x})$ maps an element to a reference cube $\boldsymbol{\xi} \in [-1,1]^3$ with logical coordinate-axes $\boldsymbol{\xi} = (\xi, \eta, \zeta)$. In this example we chose $N_{k,\xi} = 3$ and $N_{k,\eta} = 4$ LGL collocation points along ξ and η, respectively.

with determinant J and inverse $(\mathrm{J}^{-1})^j_i = \partial\xi^j/\partial x^i$. On the reference cube we choose a set of $N_{k,i}$ Legendre–Gauss–Lobatto (LGL) collocation points in each dimension i (p refinement).

Fields are represented numerically by their values at the collocation points. We denote the set of discrete values for the displacement vector field u^i within an element Ω_k as

$$\underline{u}^{i,(k)} = \left(u_1^{i,(k)}, \ldots, u_{N_k}^{i,(k)}\right), \tag{16}$$

and the collection of discrete displacement vector field values over *all* elements as $\underline{u}^i$. The values at the collocation points within an element define a three-dimensional Lagrange interpolation,

$$u^{i,(k)}(\boldsymbol{x}) := \sum_{p=1}^{N_k} u_p^i \psi_p(\boldsymbol{\xi}(\boldsymbol{x})) \quad \text{with} \quad \boldsymbol{x} \in \Omega_k, \tag{17}$$

where the basis functions $\psi_p(\boldsymbol{\xi})$ are products of Lagrange polynomials,

$$\psi_p(\boldsymbol{\xi}) := \prod_{i=1}^{3} \ell_{p_i}(\xi^i) \quad \text{with} \quad \boldsymbol{\xi} \in [-1,1]^3, \tag{18}$$

based on the collocation points in the three logical directions of the element Ω_k. Since equations (17) and (18) are local to each element, fields over the entire domain are discontinuous across element boundaries.

2.2.2. DG residuals. To formulate the elasticity equations in first-order form for the DG discretization, we use the symmetric strain S_{kl} as auxiliary variable. Following [8], we first compute the discrete auxiliary variables on the computational grid as

$$\underline{S}_{kl} = D_{(k} \cdot \underline{u}_{l)} + L \cdot ((n_{(k}\underline{u}_{l)})^* - n_{(k}\underline{u}_{l)}), \tag{19}$$

where we make use of the discrete differentiation matrix $D_i := M^{-1}MD_i$, the mass matrix

$$M_{pq} = \int_{[-1,1]^3} \psi_p(\boldsymbol{\xi})\psi_q(\boldsymbol{\xi})\,\mathrm{J}\mathrm{d}^3\xi, \tag{20}$$

the stiffness matrix

$$MD_{i,pq} = \int_{[-1,1]^3} \psi_p(\boldsymbol{\xi})\,\frac{\partial \psi_q}{\partial \xi^j}(\boldsymbol{\xi})\,(\mathrm{J}^{-1})^j_i\,\mathrm{J}\mathrm{d}^3\xi, \tag{21}$$

the lifting operator

$$ML_{pq} = \int_{[-1,1]^2} \psi_p(\boldsymbol{\xi})\psi_q(\boldsymbol{\xi})\,\mathrm{J}^{\Sigma}\mathrm{d}^2\xi, \tag{22}$$

and $L := M^{-1}ML$ on the element Ω_k [8]. The integral in equation (22) is over the boundary of the element, $\partial\Omega_k$, where n_i is the outward-pointing unit normal one-form and J^{Σ} is the surface Jacobian. The symbol $\cdot$ emphasizes matrix multiplication with the field values over the computational grid of the element. In a second step, we compute the DG residuals in strong form [8],

$$-MD_i \cdot Y^{ijkl}\underline{S}_{kl} - ML \cdot ((n_i Y^{ijkl}\underline{S}_{kl})^* - n_i Y^{ijkl}\underline{S}_{kl}) = M \cdot \underline{f}^j, \tag{23}$$

which represent the set of algebraic equations for the values $\underline{u}^i$ of the displacement vector field on the computational grid that we solve numerically.

2.2.3. Numerical flux. The quantities $(n_{(k}\underline{u}_{l)})^*$ and $(n_i Y^{ijkl}\underline{S}_{kl})^*$ in equation (23) denote a numerical flux that couples grid points across nearest-neighbor element boundaries. We employ the generalized internal-penalty numerical flux developed in [8], with one notable extension. Contrary to [8] we allow neighboring elements to define different constitutive relations, meaning $Y^{ijkl}(\boldsymbol{x})$ can be double-valued on shared element boundaries[9]. Therefore, we define the quantity

$$Y^{ijkl}_* = \frac{1}{2}\left(Y^{ijkl}_{\mathrm{int}} + Y^{ijkl}_{\mathrm{ext}}\right), \tag{24}$$

where 'int' denotes the *interior* side of an element's shared boundary with a neighbor, and 'ext' denotes the *exterior* side, i.e. the neighbor's side. With this quantity we can define the numerical flux

$$(n_{(k}\underline{u}_{l)})^* = \frac{1}{2}\left[n^{\mathrm{int}}_{(k}\underline{u}^{\mathrm{int}}_{l)} - n^{\mathrm{ext}}_{(k}\underline{u}^{\mathrm{ext}}_{l)}\right], \tag{25a}$$

$$\begin{aligned}(n_i Y^{ijkl}\underline{S}_{kl})^* = \frac{1}{2}&\left[n^{\mathrm{int}}_i Y^{ijkl}_{\mathrm{int}} D_{(k} \cdot \underline{u}^{\mathrm{int}}_{l)} - n^{\mathrm{ext}}_i Y^{ijkl}_{\mathrm{ext}} D_{(k} \cdot \underline{u}^{\mathrm{ext}}_{l)}\right] \\ &-\sigma\left[n^{\mathrm{int}}_i Y^{ijkl}_* n^{\mathrm{int}}_{(k}\underline{u}^{\mathrm{int}}_{l)} - n^{\mathrm{ext}}_i Y^{ijkl}_* n^{\mathrm{ext}}_{(k}\underline{u}^{\mathrm{ext}}_{l)}\right],\end{aligned} \tag{25b}$$

where $n^{\mathrm{ext}}_i = -n^{\mathrm{int}}_i$ for the purpose of this article. Equation (25) is the generalized internal-penalty numerical flux defined in [8], with a choice between Y^{ijkl}_{int}, Y^{ijkl}_{ext}, and Y^{ijkl}_* for every

---

[9] In the language of [8] we allow the fluxes $\mathcal{F}^i_\alpha[u_A, v_A; \boldsymbol{x}]$ to be double-valued on shared element boundaries.

occurrence of the constitutive relation. The particular choice in equation (25) ensures that the numerical flux remains consistent, meaning that $(n_i Y^{ijkl} \underline{S}_{kl})^* = -n_i^{\text{int}} T^{ij}$ when both $n_i^{\text{int}} Y^{ijkl}_{\text{int}} D_{(k} \cdot \underline{u}^{\text{int}}_{l)} = -n_i^{\text{ext}} Y^{ijkl}_{\text{ext}} D_{(k} \cdot \underline{u}^{\text{ext}}_{l)} =: -n_i^{\text{int}} T^{ij}$ and $n^{\text{int}}_{(k} \underline{u}^{\text{int}}_{l)} = -n^{\text{ext}}_{(k} \underline{u}^{\text{ext}}_{l)}$. In particular, note that the penalty term in equation (25*b*) vanishes when the displacement is continuous across the boundary, and that the numerical flux admits solutions where the stress is continuous across the boundary but the strain is not. Such solutions may arise in a layered material under stress, because the layers remain ‘glued together’ but each layer responds to the stress differently.

The penalty function in equation (25*b*) is

$$\sigma = C \, \frac{(\max(p^{\text{int}}, p^{\text{ext}}) + 1)^2}{\min(h^{\text{int}}, h^{\text{ext}})}, \tag{26}$$

where we make use of the polynomial degree p and a measure of the element size, h, orthogonal to the element boundary on either side of the interface, as detailed in [8]. We choose $C = 100$ in this article.

2.2.4. *Boundary conditions.*

We impose boundary conditions through fluxes, i.e. by a choice of exterior quantities in the numerical flux (25). Specifically, on external boundaries we set

$$(n_{(k}\underline{u}_{l)})^{\text{ext}} = (n_{(k}\underline{u}_{l)})^{\text{int}} - 2n^{\text{int}}_{(k}\underline{u}^{\text{b}}_{l)} \quad \text{and} \tag{27a}$$

$$(n_i Y^{ijkl} \underline{S}_{kl})^{\text{ext}} = (n_i Y^{ijkl} \underline{S}_{kl})^{\text{int}} + 2n_i^{\text{int}} \underline{T}^{ij}_{\text{b}}, \tag{27b}$$

where we choose either u^i_{b} to impose Dirichlet boundary conditions, or $n_i^{\text{int}} T^{ij}_{\text{b}}$ to impose Neumann boundary conditions on the boundary collocation points, and set the respective other quantity to its interior value.

For the thermal noise problem we impose the pressure induced by the laser beam,

$$n_i^{\text{int}} T^{ij}_{\text{b}} = n^j p(r), \tag{28}$$

as Neumann boundary condition on the $z = 0$ side of the cylindrical mirror, where $p(r)$ is the laser beam profile given in equation (1). On the side of the mirror facing away from the laser we impose

$$u^i_{\text{b}} = 0 \quad (\text{‘fixed’}) \tag{29}$$

as Dirichlet boundary condition, and on the mantle we impose

$$n_i^{\text{int}} T^{ij}_{\text{b}} = 0 \quad (\text{‘free’}) \tag{30}$$

as Neumann boundary condition. Equation (29) means that the back of the mirror is held in place, whereas equation (30) implies no pressure on the sides, which however, are free to deform in response to the pressure applied to the front.

2.3. *SpECTRE elliptic solver*

Once discretized, the linear algebraic equation (23) are solved numerically for the displacement vector field values $\underline{u}^i$ on all elements and grid points in the computational domain. As is typical for discretized elliptic equations, equation (23) defines a matrix equation

$$\mathcal{A}\underline{u} = \underline{b}, \tag{31}$$

where $\underline{u}$ denotes the set of all $N_{\text{DOF}} = 3 \times N_{\text{points}} = 3 \times \sum_k N_k$ displacement vector field values in the computational domain, and $\mathcal{A}$ is a matrix with $N_{\text{DOF}} \times N_{\text{DOF}}$ entries. To solve equation (31) means inverting the matrix $\mathcal{A}$. However, as the resolution of the computational domain increases, the matrix $\mathcal{A}$ easily becomes too large to construct explicitly, to store on an ordinary computer, and to invert directly.

Therefore, we solve equation (31) with the elliptic solver component of the open-source `SpECTRE` code [9, 10]. It employs an iterative generalized minimal residual (GMRES) algorithm to solve equation (31) to the requested precision. A multigrid preconditioner accelerates the GMRES algorithm by supporting each iteration with an approximate solution from a hierarchy of successively coarser grids. On every grid, an additive Schwarz smoother decomposes the problem into many overlapping subproblems, one per element in the domain, which are solved independently and in parallel. The subproblems are distributed across the cores of a computing cluster by a task-based parallelization paradigm. The elliptic solver is described in detail in [10].

3. Results

Our simulations with `SpECTRE` were performed on one or more 16-core compute nodes, each with 64 GB of memory and two eight-core Intel Haswell E5-2630v3 processors clocked at 2.40 GHz, connected with an Intel Omni-Path network. We distribute the elements that compose the computational domain evenly among cores, leaving one core per node free to perform communications.

We compare our results to previous work using an open-source finite element code to calculate the Brownian coating thermal noise for amorphous and crystalline materials. Its methods are described in sections 2.4–2.6 of [7]. The code was built using the `deal.ii` [16, 17] finite element framework and we henceforth refer to it as `deal.ii`. It adopted a standard weak form of the elastostatic equations, discretized them using a conventional finite element approach, and solved them using `deal.ii` with the `PETSc` [18] conjugate gradient linear solver and the `ParaSAILS` preconditioner in the `hypre` [19] package. The `deal.ii` code relies on the message passing interface for parallelization.

3.1. Single-coating comparison

First, we consider the single-coating scenario investigated in [7] and demonstrate the superior performance of our new approach. We choose the parameters listed in [7], table 1 for a cylindrical mirror of radius $R = 12.5$ mm with a single $d = 6.83$ μm thin effective-isotropic AlGaAs coating. We simulate the scenario both with the `deal.ii` approach employed in [7] and with our new approach with the `SpECTRE` code.

Figure 2 presents the numerical precision and computational cost of both approaches. To assess the numerical precision we successively increase the resolution in both codes. In `SpECTRE` we increase the resolution by incrementing the number of grid points in all dimensions of all elements in the domain by one, and in `deal.ii` we employ an adaptive mesh-refinement scheme [7]. We compute the error in the elastic potential energy relative to a high-resolution reference configuration simulated in `SpECTRE`, for which we have split all elements of the highest-resolution configuration included in figure 2 in half along all three dimensions (see also figure 1(a)). Hence, the high-resolution reference configuration has ~79 grid points per dimension.

We find that both codes converge to the same solution, but our new approach in `SpECTRE` achieves about four orders of magnitude higher accuracy than the `deal.ii` approach using

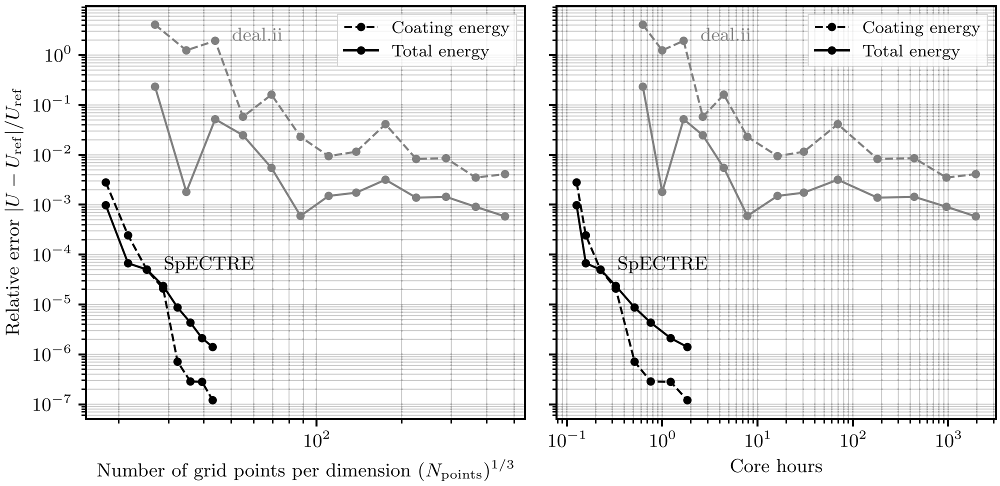

Figure 2. Relative error of the potential energy in a single amorphous coating layer (dashed lines) and in the full mirror (solid lines). Left: `SpECTRE`, with our discontinuous Galerkin method, resolves the coating layer at high precision using only a fraction of the number of grid points needed by the `deal.ii` approach. Right: `SpECTRE` solves the elliptic problem using only a fraction of the computational resources needed by the `deal.ii` approach.

the same number of grid points. Furthermore, our new approach simulates this scenario with sub-percent error in only 30 s on 15 cores, for which the `deal.ii` approach required multiple hours on 324 cores. Our new approach also achieves a fractional error below 10^{-5} in only half a core-hour, or two minutes of real time, which was prohibitively expensive with the `deal.ii` approach.

3.2. *Accuracy of the approximate analytic solution*

Second, we study the accuracy of the approximate analytic solution for the single-coating thermal noise, equation (14), using the superior numerical precision we can now achieve over the results presented in [7]. The approximate solution holds for a thin coating, $d/r_0 \ll 1$, a semi-infinite mirror, $r_0/R \ll 1$ and $d/R \ll 1$, and for isotropic-homogeneous materials. Therefore, it does not capture the finite-size effects included in our simulations, and approximates the crystalline AlGaAs coating as an amorphous material.

To assess the magnitude of the finite-size effects, we employ the simulations detailed in section 3.1, which use the same effective-isotropic model for the AlGaAs coating that underpins the approximate analytic solution. Figure 3 presents both the thermal noise computed from the simulations and the approximate analytic solution (black). Error bars are computed as $\Delta\sqrt{S_q^{\mathrm{coat}}}/\sqrt{S_q^{\mathrm{coat}}} = 1/2\,\Delta U_{\mathrm{coat}}/U_{\mathrm{coat}}$ from the relative numerical error in the elastic potential energy. While [7] estimated the magnitude of finite-size effects for this problem to 7%, we can now report that their simulations captured the effect to $7.5 \pm 0.2\%$. With our new numerical method, we can make this statement more precise and report a finite-size effect of $7.616\,649 \pm 0.000\,006\%$.

To assess the magnitude of the amorphous approximation to the crystalline coating material, we repeat the simulations with a crystalline constitutive relation and the parameters listed in [7], table 1. The thermal noise computed from these simulations is presented in figure 3 as well

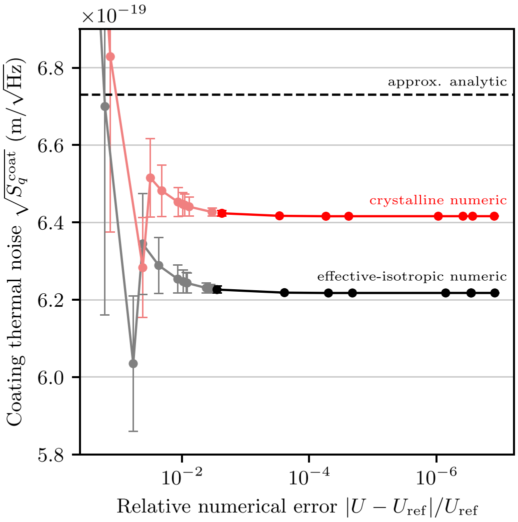

Figure 3. Thermal noise in an AlGaAs-coated mirror computed from the approximate analytic solution (14) and from our numerical simulations. The effective-isotropic simulation (black) retains the amorphous approximation for the material, but includes finite-size effects. The crystalline simulation (red) eliminates this approximation. Previous simulations with the `deal.ii` approach are shown in lighter colors to the left.

(red). We refine the estimate of 4% from [7] to 4.5 ± 0.2%, and report 4.667 990 ± 0.000 006% using our new numerical method.

Note that we report only numerical errors from our simulations here. However, the parameters that define our simulations, such as coating and substrate material properties, are typically measured experimentally and carry significant uncertainties. For example, elastic moduli recently reported in [20] were measured on the percent level. Computing the thermal noise by equation (4) also involves loss angles ϕ which can be measured on the percent level as well [20]. Therefore, computational resources are spent most effectively to drive numerical errors below sub-percent levels and no further. With our new numerical methods we achieve sub-percent accuracy with a fraction of the computational resources required before (see section 3.1).

3.3. Multiple sub-wavelength crystalline coatings

Finally, we apply our new computational approach to a scenario that presents many of the challenges we expect for applications to realistic mirror configurations. We simulate a cylindrical mirror of the same radius $R = 12.5$ mm as before, but split the $d = 6.83$ μm thin coating into nine layers, so the thickness of each coating layer is below the typical 1 μm wavelength of the laser. The coating layers alternate between fused silica and crystalline AlGaAs, with the elastic moduli c_{11}, c_{12} and c_{44} listed in [7], table 1. Neither sub-wavelength coatings nor multiple layers were simulated in [7], but our new computational approach in SpECTRE achieves both.

Figure 4 presents our numerical solution of this scenario. Our new computational approach based on DG methods resolves the thin coating layers at high accuracy without spurious oscillations. Figure 5 presents the numerical precision of the solution. We increase the resolution by incrementing the number of grid points per element and dimension and compute the relative

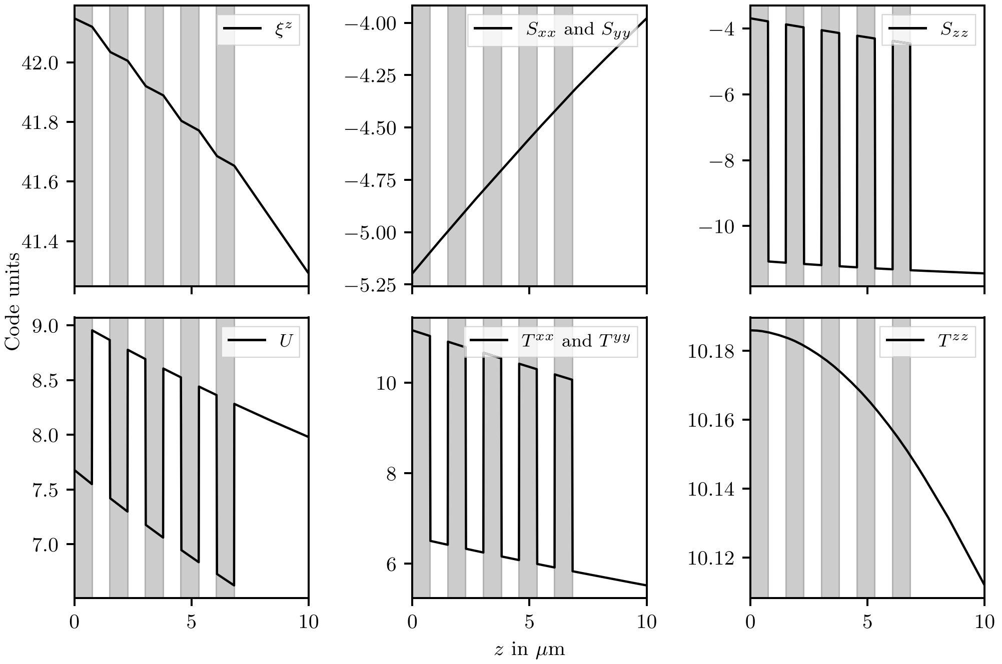

Figure 4. Elastic variables along the z-axis for a mirror with multiple thin coating layers, simulated with `SpECTRE`. Gray layers are crystalline AlGaAs, and white regions are fused silica. The nine coating layers have a combined thickness of 6.83 μm and the material extends to $z = 12.5$ mm outside the range of this plot.

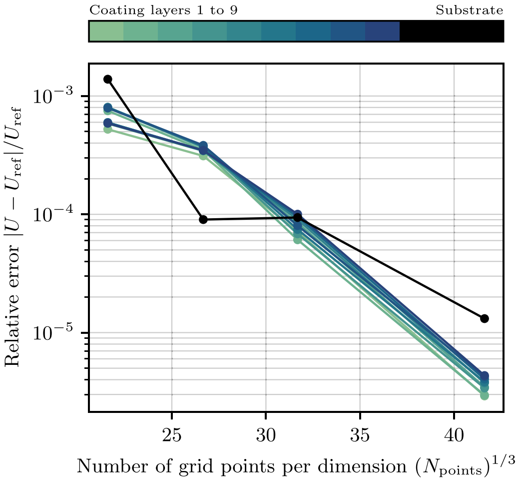

Figure 5. Convergence test of the elastic potential energy in each coating layer, and in the substrate. Our new numerical method achieves exponential convergence despite the discontinuous material properties.

error to a high-resolution reference configuration, as we did in section 3.1. The error converges exponentially, which is a feature of our DG method with grid boundaries placed at the layer interfaces.

4. Discussion

We have presented a new numerical method to model Brownian thermal noise in thin mirror coatings based on a DG discretization. With our new method, we model thermal noise in a one-inch cylindrical mirror with a microns-thick coating at unprecedented accuracy at a fraction of the time needed in a previous, conventional finite-element approach [7]. Using these high-accuracy simulations, we find that a commonly-used approximate analytic solution overestimates the coating thermal noise for this problem by 7.6% when taking only finite-size effects into account, and by 4.7% when modeling it as a crystalline material, which refines a previous estimate in [7]. We also demonstrate that, unlike the approach in [7], our new method is capable of resolving multiple sub-wavelength coatings, including coatings of a cubic-crystalline material. Our new numerical method is implemented in the open-source `SpECTRE` code and the results presented in this article are reproducible with the supplemental input-file configurations.

We found that it is crucial for the success of our new method that the interfaces between layers of different materials coincide with element boundaries in our computational domain. Then, our DG discretization with a suitable choice of numerical flux converges exponentially, achieving high accuracy with a small number of grid points. The scheme can potentially be improved in future work. Most notably, an adaptive mesh-refinement (AMR) algorithm would have great potential to further improve the accuracy and efficiency of the scheme, by distributing the resolution in the computational domain to regions and dimensions where it is most needed.

Furthermore, the elliptic solver in the `SpECTRE` code that we employ to solve the discretized problem numerically can be improved to accelerate thermal-noise calculations. The calculations we have presented in this article require a few hundred solver iterations to converge, or up to $\sim$1400 for our highest-resolution simulation with multiple sub-wavelength crystalline coatings. While simple configurations complete in seconds or minutes of real-time on 15 cores, where the previous approach needed hours on 324 cores, the more challenging configurations, which were prohibitively expensive with the previous approach, solve in about an hour on 45 cores.

We expect additional speedup with further improvements to the elliptic solver algorithm in `SpECTRE`. In particular, improvements to its multigrid preconditioner have great potential to speed up the simulations. The multigrid algorithm relies on solving the problem approximately on coarser grids to resolve large-scale modes in the solution. It currently cannot coarsen the grid any further than the size of each coating layer because the layers define the material properties. To accelerate the calculations, we intend to let the multigrid algorithm combine layers with different materials into fiducial coarse layers with effective material properties. This approach is possible because the partitioning of the domain into layers is necessary only to define material properties, not to define the cylindrical shape of the domain. Vu *et al* [10] shows that the multigrid algorithm can achieve resolution-independent iteration counts when the domain can be coarsened sufficiently. Note that the fiducial coarse layers affect only the convergence speed of the solver and do not change the solution once the solver has converged.

Our numerical models of thermal noise have the potential to inform upgrades that increase the sensitivity of gravitational-wave detectors, using the advanced computational technology that we develop for numerical-relativity simulations in the `SpECTRE` code. In the future, we intend to apply our new numerical method to simulate Brownian thermal noise in more realistic mirror configurations and materials that are under consideration for current and future gravitational-wave detectors, such as the optimized configuration found in [21]. While approximate analytic solutions can provide useful estimates, only numerical models can precisely quantify the finite-size effects of changing the mirror geometry. In particular, finite-size effects are more important for real gravitational-wave detectors than for tabletop experiments measuring thermal noise. Tabletop experiments often use small beam sizes to enlarge the thermal noise and hence make it easier to measure, whereas gravitational-wave detectors prefer large beam sizes to minimize thermal noise. Therefore, we plan to employ our new numerical method to explore realistic mirror configurations, with the goal of finding configurations that minimize Brownian coating thermal noise.

Data availability statement

All data that support the findings of this study are included within the article (and any supplementary files).

Acknowledgments

The authors thank Josh Smith for helpful discussions. Computations were performed with the `SpECTRE` [9] and `deal.ii` [16, 17] codes on the `Minerva` cluster at the Max Planck Institute for Gravitational Physics and on the `Ocean` cluster at Fullerton. The figures in this article were produced with `dgpy` [22], `matplotlib` [23, 24], `TikZ` [25] and `ParaView` [26]. This work was supported in part by the Sherman Fairchild Foundation, by NSF Grant Nos. PHY-1654359 and AST-1559694 at Cal State Fullerton, by NSF Grant Nos. PHY-2011961, PHY-2011968 and OAC-1931266 at Caltech and by NSF Grant Nos. PHY-1912081 and OAC-1931280 at Cornell.

ORCID iDs

Nils L Vu https://orcid.org/0000-0002-5767-3949
Samuel Rodriguez https://orcid.org/0000-0002-1879-8810
Tom Włodarczyk https://orcid.org/0000-0003-0005-348X
Geoffrey Lovelace https://orcid.org/0000-0002-7084-1070
Harald P Pfeiffer https://orcid.org/0000-0001-9288-519X
Gabriel S Bonilla https://orcid.org/0000-0003-4502-528X
Nils Deppe https://orcid.org/0000-0003-4557-4115
François Hébert https://orcid.org/0000-0001-9009-6955
Lawrence E Kidder https://orcid.org/0000-0001-5392-7342
Jordan Moxon https://orcid.org/0000-0001-9891-8677
William Throwe https://orcid.org/0000-0001-5059-4378

References

[1] Barsotti L, McCuller L, Evans M and Fritschel P 2018 The A+ design curve *Technical Report* T1800042-v5 (LIGO Document)
[2] Cole G D, Zhang W, Martin M J, Ye J and Aspelmeyer M 2013 *Nat. Photon.* **7** 644–50
[3] Levin Y 1998 *Phys. Rev.* D **57** 659–63
[4] Callen H B and Welton T A 1951 *Phys. Rev.* **83** 34
[5] Bernard W and Callen H B 1959 *Rev. Mod. Phys.* **31** 1017
[6] Kubo R 1966 *Rep. Prog. Phys.* **29** 255
[7] Lovelace G, Demos N and Khan H 2018 *Class. Quantum Grav.* **35** 025017
[8] Fischer N L and Pfeiffer H P 2022 *Phys. Rev.* D **105** 024034
[9] Deppe N *et al* 2022 SpECTRE v2022.02.17 (https://doi.org/10.5281/zenodo.6127519)

[10] Vu N L *et al* 2022 *Phys. Rev.* D **105** 084027
[11] Kale L *et al* 2019 The Charm++ parallel programming system (available at: https://charm.cs.illinois.edu)
[12] Kidder L E *et al* 2017 *J. Comput. Phys.* **335** 84–114
[13] Thorne K S and Blandford R D 2017 *Modern Classical Physics* (Princeton, NJ: Princeton University Press)
[14] Harry G M *et al* 2002 *Class. Quantum Grav.* **19** 897–917
[15] Hong T, Yang H, Gustafson E K, Adhikari R X and Chen Y 2013 *Phys. Rev.* D **87** 082001
[16] Arndt D *et al* 2021 *J. Numer. Math.* **29** 171–86
[17] Arndt D, Bangerth W, Davydov D, Heister T, Heltai L, Kronbichler M, Maier M, Pelteret J P, Turcksin B and Wells D 2021 *Comput. Math. Appl.* **81** 40–422
[18] Balay S *et al* 2021 PETSc (available at: www.mcs.anl.gov/petsc)
[19] Falgout R D, Jones J E and Yang U M 2006 The design and implementation of hypre, a library of parallel high performance preconditioners *Numerical Solution of Partial Differential Equations on Parallel Computers* (Berlin: Springer) pp 267–94
[20] Amato A *et al* 2021 *Phys. Rev.* D **103** 072001
[21] Venugopalan G, Arai K and Adhikari R X 2021 Global optimization of multilayer dielectric coatings for precision measurements (arXiv:2110.13437)
[22] Vu N L 2021 dgpy (https://doi.org/10.5281/zenodo.5086181)
[23] Hunter J D 2007 *Comput. Sci. Eng.* **9** 90–95
[24] Caswell T A *et al* 2020 matplotlib (https://doi.org/10.5281/zenodo.4268928)
[25] Tantau T 2021 pgf—a portable graphic format for TeX (available at: https://github.com/pgf-tikz/pgf)
[26] Ahrens J, Geveci B and Law C 2005 *Paraview: An End-User Tool for Large-Data Visualization Visualization Handbook* (Burlington, VT: Butterworth-Heinemann)